COMMUNICATION

Aramid nanofiber–poly(vinyl alcohol) composite gel polymer electrolytes for lithium chloride-based supercapacitors

Yuseung Choi,†[a] Gilyong Shin,†[a,b] Eun Jae Nam,[a] Ji Heon Hong,[a] Byeong Jun So[a] and Tae June Kang [ID] *[a]

Gel polymer electrolytes (GPEs) are key components in electrochemical energy-storage devices, as they simultaneously serve as ion-conducting media and separators. However, their performance is often limited by the trade-off between mechanical robustness and ionic conductivity, which becomes particularly problematic in highly concentrated aqueous electrolytes due to electrolyte-induced dimensional instability. Here, we report a composite GPE based on a rigid aramid nanofiber (ANF) network coated with a hydrophilic poly(vinyl alcohol) (PVA) layer, designed for compatibility with water-in-salt electrolyte systems. The ANF scaffold provides a high-modulus framework for dimensional stability, while hydrogen-bonding interactions at the ANF–PVA interface enable effective stress redistribution without significantly impeding ion transport. The ANF–PVA composite hydrogel was impregnated with a lithium chloride-based water-in-salt electrolyte to form a GPE and subsequently coated onto activated-carbon-decorated carbon-fiber electrodes to fabricate supercapacitors. The resulting devices exhibit stable electric double-layer capacitive behavior, reliable rate capability, and excellent cycling stability over a wide temperature range from −20 to 50 °C, together with scalable electrochemical performance upon increasing device length. These results highlight the effectiveness of composite polymer-network engineering for mechanically robust and ionically efficient aqueous GPEs suitable for low-temperature energy-storage applications.

1. Introduction

Electrochemical energy-storage devices for wearable and deformable systems[1–3] require electrolytes that simultaneously provide efficient ionic transport, reliable electrical insulation between electrodes, and mechanical integrity under deformation. Gel polymer electrolytes (GPEs)[4,5] are particularly appealing in this context because they integrate the functions of electrolyte and separator into a single, mechanically continuous layer. By confining an aqueous electrolyte within a polymer network, GPEs suppress electrolyte leakage and allow the gel itself to physically isolate the electrodes, eliminating the need for an additional porous separator. Such separator-free configurations reduce inactive thickness, shorten ion-transport distances, and lower internal resistance, thereby decreasing polarization losses and enhancing rate performance in compact and mechanically compliant energy-storage devices.[6]

Despite these advantages, the performance of GPEs is governed by a fundamental coupling between mechanical integrity and ionic transport properties.[7,8] To effectively prevent electrical shorting in thin and deformable configurations, GPEs must maintain sufficient modulus, toughness, and dimensional stability. These properties are typically enhanced by increasing polymer content,[4,9] cross-link density,[10] or inter-chain interactions;[8,11] however, such strategies inevitably restrict polymer segmental dynamics and narrow ion-transport pathways, leading to diminished ionic conductivity.[7,9] In contrast, highly swollen polymer networks promote rapid ion transport but often lack the mechanical robustness required to maintain stable electrode separation under mechanical perturbation.[12] This coupling becomes more pronounced in aqueous GPEs, where freezing at sub-zero temperatures suppresses ionic mobility and induces mechanically disruptive phase transitions that compromise both structural integrity and electrochemical performance. As a result, recent studies have increasingly explored hierarchical,[13,14] composite,[7,15] or multi-network gel architectures[8,11,12] that redistribute mechanical reinforcement and ion-transport functionality across distinct structural components.

Beyond polymer network design alone, electrolyte chemistry provides an additional avenue to mitigate low-temperature limitations. Water-in-salt electrolytes (WISEs),[16,17] characterized by

[a]Department of Mechanical Engineering, Inha University, Incheon 22212, South Korea.
E-mail: tjkang@inha.ac.kr
[b]Department of Aeronautics and Astronautics, Stanford University, Stanford, CA 94305, USA
† These authors contributed equally.

highly concentrated salt solutions, reduce the activity of free water and depress freezing while maintaining relatively high ionic conductivity. These features make WISEs promising candidates for sub-zero aqueous energy-storage systems and motivate their incorporation into gel polymer electrolytes.[4,18,19] However, within GPE matrices, the extreme ionic strength of WISEs can amplify ion-specific interactions between solvated ions and polymer chains, leading to changes in polymer hydration and chain conformation, often discussed in the context of Hofmeister-type ion specificity.[20–22] In hydroxyl-rich polymer matrices that rely on extensive hydrogen bonding for structural cohesion, ion–dipole interactions and competition for bound water can strongly perturb polymer hydration. Poly(vinyl alcohol) (PVA), a representative hydroxyl-rich gel polymer, is particularly susceptible to such effects, which can alter gel swelling and mechanical response and may result in softening, embrittlement, or partial loss of structural continuity under WISE conditions. These limitations highlight the need for GPE architectures that remain mechanically coherent in highly concentrated aqueous electrolytes.

In this work, we address this challenge by developing a composite GPE architecture consisting of a rigid aramid nanofiber (ANF) scaffold combined with a hydrophilic PVA coating layer. The ANF network forms a continuous, high-modulus framework that provides dimensional stability and resistance to mechanical deformation, while the PVA phase establishes dynamic hydrogen-bonded interactions with the ANF surface, enabling effective stress redistribution without compromising ion-accessible pathways. Importantly, because PVA functions here as a conformal interfacial phase rather than a standalone matrix, the ANF–PVA composite maintains structural integrity in highly concentrated aqueous electrolytes, including lithium chloride-based WISE electrolytes, consistent with the swelling tests in Fig. S1. By integrating this composite polymer host with LiCl-based WISE electrolytes, we demonstrate an ANF–PVA composite GPE that preserves structural stability and ionic conduction even at low temperatures.

2. Experimental section

2.1 Materials

Poly(p-phenylene terephthalamide) (PPTA) fibers (Alkex AF-3000, Hyosung Advanced Materials), dimethyl sulfoxide (DMSO, >99.5%, Daejung), potassium hydroxide (KOH, Sigma-Aldrich), and poly(vinyl alcohol) (PVA, 99+% hydrolyzed, M_w = 146 000–186 000, Sigma-Aldrich) were used for the preparation of GPEs. Lithium chloride (LiCl, >99%, Sigma-Aldrich) was employed as the salt source for water-in-salt electrolytes, and deionized (DI) water was used throughout the experiments. Activated carbon (AC, Brunauer–Emmett–Teller surface area: 1360 m^2 g^{-1}, US Research Nanomaterials, Inc.), multiwalled carbon nanotubes (MWCNTs, 95%, outer diameter <7 nm, US Research Nanomaterials, Inc.), and poly(vinylidene fluoride) (PVDF, average M_w ~ 534 000, Sigma-Aldrich) were used for electrode fabrication. N-Methyl-2-pyrrolidone (NMP, Daejung)

served as the slurry solvent. Carbon fiber tows (Tansome H2250-12K, Hyosung Advanced Materials) were used as current collectors.

2.2 Preparation of ANF dispersions

ANF dispersions were prepared using a top-down fibrillation method, following a procedure originally reported in the literature[23–25] with minor modifications. To obtain a high-concentration ANF dispersion suitable for forming densely cross-linked ANF networks in GPEs, water was introduced as a co-solvent into the DMSO system. The presence of water enhances the solubility of KOH in DMSO and reduces the viscosity of the dispersion medium, thereby promoting efficient deprotonation and fibrillation of PPTA fibers. For the preparation of a 1.0 wt% ANF dispersion containing 100 mg of ANFs, 93.6 g of DMSO, 1.5 g of KOH, 1.0 g of PPTA fibers, and 3.9 g of DI water were added to a glass bottle. Prior to mixing, the bottle was purged with nitrogen gas to minimize the influence of ambient moisture. The mixture was magnetically stirred at room temperature for 6 h until complete fibrillation of the PPTA fibers was achieved. The resulting ANF dispersion exhibited a characteristic reddish coloration (Fig. S2A). Atomic force microscopy (AFM) analysis confirmed the formation of fibrillated ANFs with an average diameter of approximately 14 nm (Fig. S2B and S2C).

2.3 Preparation of PVA solutions

DMSO was selected as the solvent for dissolving PVA because its aprotic and highly polar nature suppresses undesired aggregation or structural recovery of ANFs during subsequent mixing,[26–28] thereby enabling homogeneous blending. To prepare PVA/DMSO solutions with PVA weight fractions of 3, 5, and 10 wt%, DMSO was heated to 60 °C under magnetic stirring, and PVA was gradually added until complete dissolution and the target composition were achieved. The resulting PVA solutions remained optically transparent over the entire concentration range, while their viscosity increased with increasing PVA content.

2.4 Preparation of ANF–PVA composite hydrogels and ANF hydrogels

ANF–PVA composite hydrogels were prepared by mixing equal masses of a 1.0 wt% ANF/DMSO dispersion and PVA/DMSO solutions with PVA contents of 3, 5, or 10 wt% in a glass container. The mixtures were homogenized using a planetary centrifugal mixer at 2000 rpm for 5 min, followed by a defoaming step at 2200 rpm for 30 s. The resulting mixtures became progressively more transparent with increasing PVA content, and no visible aggregation was observed. The ANF/PVA/DMSO mixtures were subsequently cast into glass molds and immersed in DI water to induce reprotonation of the ANFs and promote the reformation of hydrogen-bonded nanofiber networks. After reprotonation, the resulting ANF–PVA hydrogels exhibited a gradual color transition from reddish to yellowish tones and became increasingly whitish and transparent with increasing PVA content (Fig. S3A). The hydrogels were denoted as AP3,

AP5, and AP10 according to the PVA/DMSO weight fractions employed. For comparison, an ANF hydrogel without PVA was prepared by subjecting the 1.0 wt% ANF/DMSO dispersion to a defoaming step at 2200 rpm for 30 s, followed by casting into a glass mold and immersion in DI water using the same reprotonation procedure. This sample served as a reference ANF hydrogel. The resulting ANF hydrogel exhibited a more intense yellow coloration than the ANF–PVA hydrogels (Fig. S3B).

2.5 Preparation of PVA hydrogels

PVA hydrogels were prepared using a freeze–thaw method. 5.0 g of PVA was gradually added to 95 g of DI water maintained at 80 °C under continuous magnetic stirring. The mixture was stirred for 6 h until a homogeneous PVA/H_2O solution was obtained. The resulting solution was poured into a polystyrene mold and subjected to repeated freeze–thaw cycles consisting of freezing at −20 °C for 8 h followed by thawing at 25 °C for 16 h. This freeze–thaw process was repeated five times. During these cycles, physical crosslinking points formed through crystallite formation and intermolecular interactions between PVA chains, resulting in the establishment of a hydrogel network.

2.6 Preparation of functionalized carbon fiber tows

Carbon fiber tows were used as current collectors owing to their high electrical conductivity and favorable mechanical properties.[29–31] To increase the effective surface area for electric double-layer charge storage,[32,33] AC was deposited onto the carbon fiber tows using a previously reported roll-to-roll slurry coating and drying process.[34] The electrode slurry was prepared by mixing AC, MWCNTs, and PVDF binder at a weight ratio of 8 : 1 : 1. NMP was then added at 7.5 times the total solid content to obtain a coatable slurry. The mixture was dispersed using a thin-film mixer at 18 000 rpm for 1.0 min to form a homogeneous slurry. Prior to coating, carbon fiber tows were treated by corona discharge to improve surface wettability and interfacial adhesion. The treated tows were spread using a lab-built reel-to-reel system, coated with the electrode slurry, and recollected to enable uniform deposition throughout the tow interior. The coated tows were dried in a vacuum oven at 80 °C for 12 h. The resulting electrodes exhibited an average mass loading of 4.0 mg cm^{-1} and are hereafter referred to as functionalized tows (F-tows).

2.7 Fabrication of fiber-shaped supercapacitors

To fabricate fiber-shaped supercapacitors, F-tows were first impregnated with ANF/PVA precursor solutions *via* a dip-coating process. The F-tow electrodes were immersed in ANF/PVA/DMSO mixtures and withdrawn at a controlled rate of 1.0 cm s^{-1} to achieve uniform coating along the fiber length. The coated F-tows were then immersed in DI water to induce reprotonation of the ANFs and promote reassembly of the ANF–PVA network. During this process, DMSO was replaced by water and residual KOH was removed, resulting in the formation of a conformal ANF–PVA hydrogel layer on the F-tow surface. This approach enables direct formation of the GPE

coating on the fiber electrode, in contrast to multistep freeze–thaw processing typically used for standalone PVA hydrogels. Following hydrogel formation, the F-tows were immersed in a 25 wt% LiCl aqueous electrolyte to replace the water within the hydrogel network. This soaking process enabled solvent exchange and uniform electrolyte impregnation throughout the hydrogel layer, yielding an ANF–PVA-based GPE coating on the F-tows. Two GPE-coated tows were subsequently assembled in a stacked configuration to form a symmetric fiber-shaped supercapacitor and encapsulated with a polyimide film to minimize electrolyte composition changes due to evaporation and moisture absorption.

2.8 Characterization and instrumentation

Planetary centrifugal mixing of ANF/PVA precursor solutions was carried out using a mixer (ARE-310, Thinky), and thin-film slurry mixing for electrode slurry preparation was performed using a thin-film mixer (FM-40-L, Frimix). The ionic conductivity of LiCl aqueous electrolytes was measured at 25 °C using an ionic conductivity meter (SevenCompact™ S230, Mettler-Toledo) with a solution volume of 20 mL. The morphology of ANFs was characterized by AFM (Nanoscope Multimode IVa, Bruker). Diluted ANF dispersions were deposited onto oxygen plasma-treated glass substrates, dried at 60 °C, and imaged in tapping mode over a scan area of 5 × 5 μm^2. AFM images were then processed using Nanoscope software. Attenuated total reflection Fourier transform infrared (ATR-FTIR) spectroscopy (VERTEX80V, Bruker) was used to investigate hydrogen-bonding interactions between ANFs and PVA. Spectra were collected with 16 scans at a resolution of 4 cm^{-1} over the range of 4000 to 800 cm^{-1} after vacuum drying. Elemental compositions were analyzed by energy-dispersive X-ray spectroscopy (EDS, S-4300SE, Hitachi) after freeze-drying the hydrogel samples. Freeze-drying was performed using a lyophilizer (TFD8503, Ilshin BioBase). Thermogravimetric analysis (TGA, N1000, Scinco) was performed under a nitrogen atmosphere from room temperature to 900 °C at a heating rate of 10 °C min^{-1}. Mechanical properties of hydrogels were evaluated using a universal testing machine (JSV-H1000, Japan Instrumentation System Co.) equipped with a 10 N load cell. Tensile tests were conducted at a crosshead speed of 10 mm min^{-1} using ASTM D638 Type V specimens. Lap shear tests of functionalized fiber tows were performed at a displacement rate of 10 mm min^{-1} using the same instrument. All mechanical tests were carried out at 25 °C and 60% relative humidity. Morphological characterization of pristine carbon fiber tows, functionalized tows, and hydrogel-coated tows was conducted using scanning electron microscopy (SEM, CX-200TM, COXEM). Cross-sectional and porous structures of hydrogels were examined by high-resolution field-emission SEM (FE-SEM, S-4300SE, Hitachi) after freeze-drying. Electrochemical measurements were performed using an electrochemical workstation (CS310, Corrtest Instruments). Electrolyte-coated fiber tows were characterized in a three-electrode half-cell setup with a carbon-felt counter electrode and an Ag/AgCl reference elec-

trode in 25 wt% LiCl aqueous electrolyte. Fiber-shaped supercapacitors were evaluated by cyclic voltammetry (CV), electrochemical impedance spectroscopy (EIS), and galvanostatic charge–discharge (GCD) measurements over a temperature range from −20 to 50 °C.

3.   Results and discussion

3.1   ANF–PVA composite hydrogels

Fig. 1A schematically illustrates the fabrication of ANF and ANF–PVA (AP) composite hydrogels. The detailed experimental
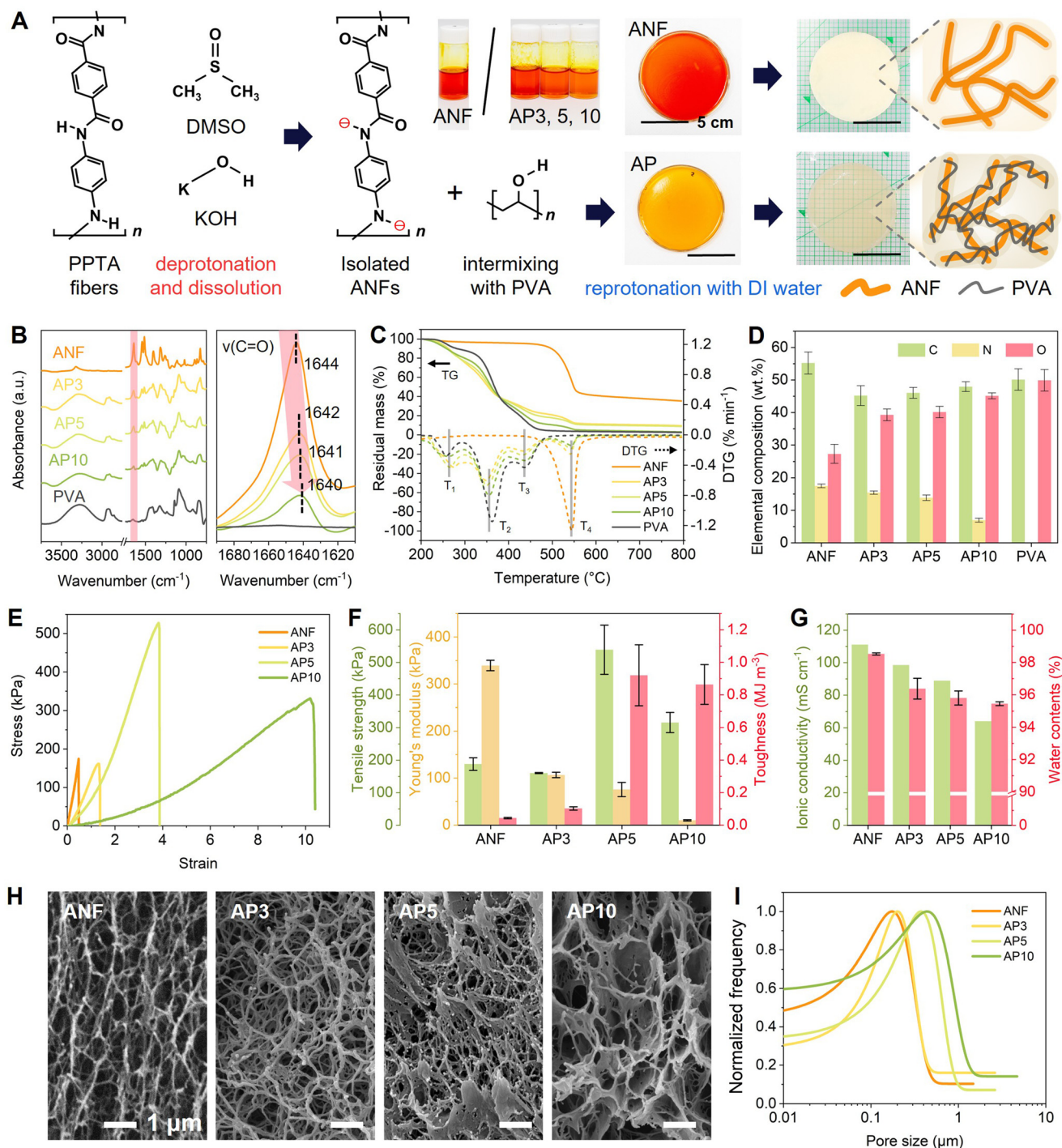

Fig. 1   (A) Schematic illustration of the preparation of ANF and AP hydrogels. (B) FT-IR spectra, (C) TG/DTG curves, and (D) elemental composition analysis of ANF, PVA, and AP hydrogels. (E) Tensile stress–strain curves and (F) corresponding mechanical properties of the hydrogels. (G) Ionic conductivity and water content of ANF and AP hydrogels. (H) SEM images showing hydrogel microstructures and (I) the corresponding pore-size distributions.

procedures are described in the Experimental section. Briefly, ANF dispersions were prepared *via* a top-down deprotonation and fibrillation process of macroscale PPTA fibers in a DMSO/KOH system. Deprotonation of the amide N–H groups disrupts the strong interchain hydrogen bonding in PPTA, enabling exfoliation of the fibers into individualized ANFs that remain stably dispersed in DMSO. For ANF hydrogels, the dispersion was cast and subsequently immersed in DI water. Solvent exchange from DMSO to water induces reprotonation of the deprotonated amide groups, restoring inter- and intra-molecular hydrogen bonding between adjacent ANFs. This reprotonation-driven reassembly leads to spontaneous self-organization of the nanofibers into a ANF hydrogel network. In contrast, AP hydrogels were fabricated by first mixing the ANF dispersion with PVA solutions in DMSO prior to casting. The AP hydrogels were denoted as AP3, AP5, and AP10, corresponding to PVA weight fractions of 3, 5, and 10 wt% in the precursor DMSO solutions, respectively. Upon immersion in DI water, reprotonation of ANFs occurs concurrently with the formation of hydrogen bonds between ANF carbonyl groups and hydroxyl groups on PVA chains. This coupled process yields an interpenetrating, hydrogen-bonded composite network in which the rigid ANF scaffold is integrated with the flexible PVA phase.

FT-IR spectroscopy was employed to examine intermolecular interactions within the hydrogels (Fig. 1B and full spectra in Fig. S4). While the spectra of the AP hydrogels display characteristic features of both ANF[35–37] and PVA,[38,39] a magnified view of the carbonyl (C=O) stretching region reveals a gradual redshift of the aramid C=O band in the AP hydrogels relative to the ANF hydrogel. Specifically, the C=O stretching peak shifts from 1644 cm^{-1} for ANF to 1640 cm^{-1} for AP10 as the PVA content increases. This systematic redshift suggests progressively strengthened hydrogen-bonding interactions between ANF carbonyl groups and hydroxyl groups on PVA chains.[38,40,41] Such composition-dependent evolution of the C=O stretching vibration is consistent with enhanced interfacial interactions between the rigid ANF network and the flexible PVA phase.

Fig. 1C shows the results of TGA analysis to further corroborate the compositional integrity of the AP hydrogels. The ANF hydrogel exhibits a dominant high-temperature derivative thermogravimetric (DTG) peak at $T_4 \sim 550$ °C, attributed to cleavage of the aromatic amide backbone of ANFs.[42] In contrast, PVA and AP hydrogels display a PVA-related DTG peak at $T_1 \sim 250$ °C, associated with dehydration and thermolysis of unstable side groups.[43] The AP hydrogels additionally exhibit two PVA-derived degradation steps at T_2 (300–450 °C) and T_3 (450–550 °C), corresponding to PVA backbone decomposition and subsequent degradation of polyene residues, respectively.[44] The relative intensities and associated mass losses of these PVA- and ANF-derived features vary systematically with composition (Table S1), indicating that the thermal decomposition behavior of the AP hydrogels reflects the ANF/PVA weight ratios defined during synthesis.

Elemental analysis by energy-dispersive X-ray spectroscopy (EDS) provides complementary support for this compositional trend (Fig. 1D and Table S2). While the ANF hydrogel contains C, N, and O and the PVA hydrogel contains only C and O, the nitrogen content of the AP hydrogels decreases monotonically with increasing PVA fraction, consistent with the progressive dilution of the ANF component inferred from the TGA results.

Fig. 1E shows the mechanical properties of the fabricated hydrogels, evaluated by tensile testing in the hydrated state. The pristine ANF hydrogel exhibits an average fracture strain of 48.5% and a tensile strength of 188.7 kPa, which can be attributed to a randomly assembled nanofiber network with a limited density of effective load-bearing junctions. Upon incorporation of PVA, the fracture strain increases markedly to 136.3% (AP3), 386.7% (AP5), and 960.1% (AP10), indicating a pronounced enhancement in deformability across the AP samples. For tensile strength, while AP3 shows a tensile strength of 160.6 kPa, comparable to that of the pristine ANF hydrogel, AP5 exhibits a substantial increase to 539.3 kPa. Upon further increase in PVA content, the tensile strength decreases to 316.5 kPa for AP10, yet remains higher than that of the ANF hydrogel. Accordingly, the toughness increases from 0.102 MJ m^{-3} (AP3) to 0.92 MJ m^{-3} (AP5) and remains high at 0.86 MJ m^{-3} (AP10), representing a substantial enhancement relative to ANF (0.0429 MJ m^{-3}) (Fig. 1F and Table S3). Young's modulus decreases monotonically with increasing PVA content (339.3, 106.7, 75.7, and 10.0 kPa for ANF, AP3, AP5, and AP10, respectively), consistent with progressive softening as the compliant PVA polymer fraction increases.

This mechanical evolution is consistent with PVA acting as a compliant secondary phase that bridges adjacent ANFs through hydrogen-bonding interactions, thereby facilitating stress redistribution and energy dissipation during deformation.[38,45–47] At lower PVA content (AP3), the primary effect is enhanced extensibility with only minor changes in strength, whereas at higher PVA contents (AP5 and AP10) large gains in fracture strain and toughness are achieved. Meanwhile, Young's modulus decreases monotonically with increasing PVA fraction, reflecting progressive softening of the composite network as the contribution of the mechanically compliant PVA phase becomes more pronounced.

To assess the suitability of the AP hydrogels as GPE hosts, ionic conductivity and water content were evaluated, as shown in Fig. 1G. Both parameters decrease gradually with increasing PVA content, consistent with increased polymer solid content and network densification that reduce the fraction of free water and partially constrain percolating transport pathways. Nevertheless, the AP hydrogels retain high ionic conductivity and water content: AP3 exhibits ~98.5 mS cm^{-1} and ~96.4% water content, AP5 ~88.9 mS cm^{-1} and ~95.8%, and AP10 ~64.1 mS cm^{-1} and ~95.4%, indicating that hydrated ion-transport pathways remain continuous across the AP samples.

Fig. 1H presents SEM images that provide microstructural context for the observed mechanical properties and ion-transport characteristics. The ANF hydrogel consists of a randomly

entangled nanofiber network with abundant submicron-scale pores, which facilitates water uptake and ion transport but provides relatively limited load-bearing junction density. With increasing PVA content, ANF surfaces become progressively coated. The polymer-mediated bridges form between adjacent ANFs might improve stress transfer and introducing a more compliant, energy-dissipative interfacial phase. Concurrently, the pore architecture evolves, and quantitative analysis (Fig. 1I) reveals an increase in average pore size from ∼0.17 μm for ANF to ∼0.46 μm for AP10, accompanied by a decrease in overall porosity, consistent with preferential loss or partial filling of smaller pores. This microstructural evolution provides a structural basis for the composition-dependent balance between enhanced mechanical toughness and gradually reduced ionic conductivity and water content.

3.2 AC-functionalized carbon fiber electrodes with AP hydrogel coatings

To evaluate the applicability of the proposed AP composite hydrogels as a GPE in supercapacitor devices, carbon fiber tows were employed as current collectors and functionalized with an electrode slurry containing AC, MWCNTs, and a PVDF binder at a controlled ratio, as described in detail in the Experimental section. Fig. 2A schematically illustrates the fabrication process, including AC slurry coating on carbon fiber tows using a lab-built roll-to-roll system, followed by ANF/PVA gel dip-coating. SEM images of the pristine and AC-functionalized carbon fiber tows or F-tows are shown in Fig. 2B. The images confirm that the AC-based electrode materials are uniformly adhered to and distributed throughout both the surface and interior of the carbon fiber tows, indicating effective slurry infiltration and homogeneous electrode formation.

Following electrode functionalization, the ANF/PVA precursor solution was applied to the F-tows by dip-coating and subsequently converted into a hydrogel network through solvent exchange-induced gelation, as described in the Experimental section. This process involves reprotonation of the ANFs and the formation of a hydrogen-bonded AP network. Fig. 2C presents SEM images of the resulting structures, revealing that the AP hydrogel forms a continuous and conformal coating with a thickness of several micrometers along the electrode surface. This thin and conformal hydrogel coating effectively electrically isolates the opposing electrodes while preserving short ion-transport distances, thereby enabling high-rate electrochemical operation.

The effect of AP hydrogel coating on the electrochemical behavior of F-tow electrodes was evaluated using a three-electrode half-cell configuration with a carbon-felt counter electrode and an Ag/AgCl reference electrode in 25 wt% LiCl aqueous electrolyte. Representative cyclic voltammograms recorded at 10 mV s^{-1} are shown in Fig. 2D (see also Fig. S5 for scan rates from 5 to 100 mV s^{-1}). Although the AP-coated F-tows exhibit slightly lower capacitance values than the uncoated F-tow, which can be attributed to additional ionic transport resistance introduced by the ANF–PVA hydrogel layer, all electrodes maintain quasi-rectangular CV profiles charac-

teristic of electric double-layer capacitive behavior, indicating that the hydrogel coating does not alter the underlying charge-storage mechanism.

The scan-rate-dependent specific and gravimetric capacitances are summarized in Fig. 2E. Consistent with the CV results, the AP-coated F-tows retain a substantial fraction of the capacitance and rate capability of the uncoated electrode across the entire scan-rate range, demonstrating that the thin and conformal hydrogel layer does not impose pronounced kinetic limitations on ion transport during dynamic operation.

Charge-storage kinetics were further assessed by power-law analysis of the CV data (Fig. 2F). The uncoated F-tow exhibits a b-value of approximately 0.87, whereas the b-values decrease gradually to 0.71 (AP3), 0.69 (AP5), and 0.65 (AP10) with increasing PVA content. This behavior is attributed primarily to the increased polymer solid fraction in the AP hydrogel matrix at higher PVA contents, which partially restricts effective ion-transport pathways and increases diffusion-influenced contributions to charge storage. Nonetheless, the relatively high b-values (>0.5) maintained for all AP-coated electrodes indicate that capacitive charge storage remains dominant. This result suggests that the thin AP hydrogel layer still provides efficient ionic access to the electrode surface despite composition-dependent reductions in bulk ionic conductivity.

In addition to enabling efficient ion transport, GPEs must suppress electrical shorting induced by mechanical deformation and maintain stable interfacial contact with electrodes during operation. Accordingly, strong interfacial adhesion and mechanical integrity at the electrolyte–electrode interface are essential for reliable device performance. To assess interfacial adhesion, lap shear tests were conducted by bonding two F-tows using ANF and AP hydrogels. As evidenced by the lap shear stress-displacement curves in Fig. 2G, the ANF and AP3 hydrogels show early interfacial separation accompanied by fracture of the electrolyte layer at relatively small displacements. In contrast, the AP10 hydrogel does not exhibit pronounced interfacial debonding; instead, failure occurs predominantly through cohesive deformation within the hydrogel. Notably, the AP5 hydrogel exhibits a balanced response, combining sufficient shear strength with stable interfacial integrity, resulting in the highest effective adhesion performance among the tested compositions (Fig. 2H and Table S4). Based on the combined assessment of mechanical properties, electrochemical performance, and interfacial adhesion behavior on F-tow electrodes, the AP5 composition was selected as a representative GPE for subsequent fiber-shaped supercapacitor device evaluations.

3.3 Performance evaluation of fiber-shaped supercapacitors with ANF–PVA GPE

The separator-free configuration enabled by the GPE simplifies device architecture and is particularly advantageous for fiber-shaped energy-storage systems, where compact geometry, mechanical robustness, and stable electrode–electrolyte interfaces are essential. Fig. 3A shows a schematic diagram and optical images of the fabricated fiber-shaped supercapacitor.
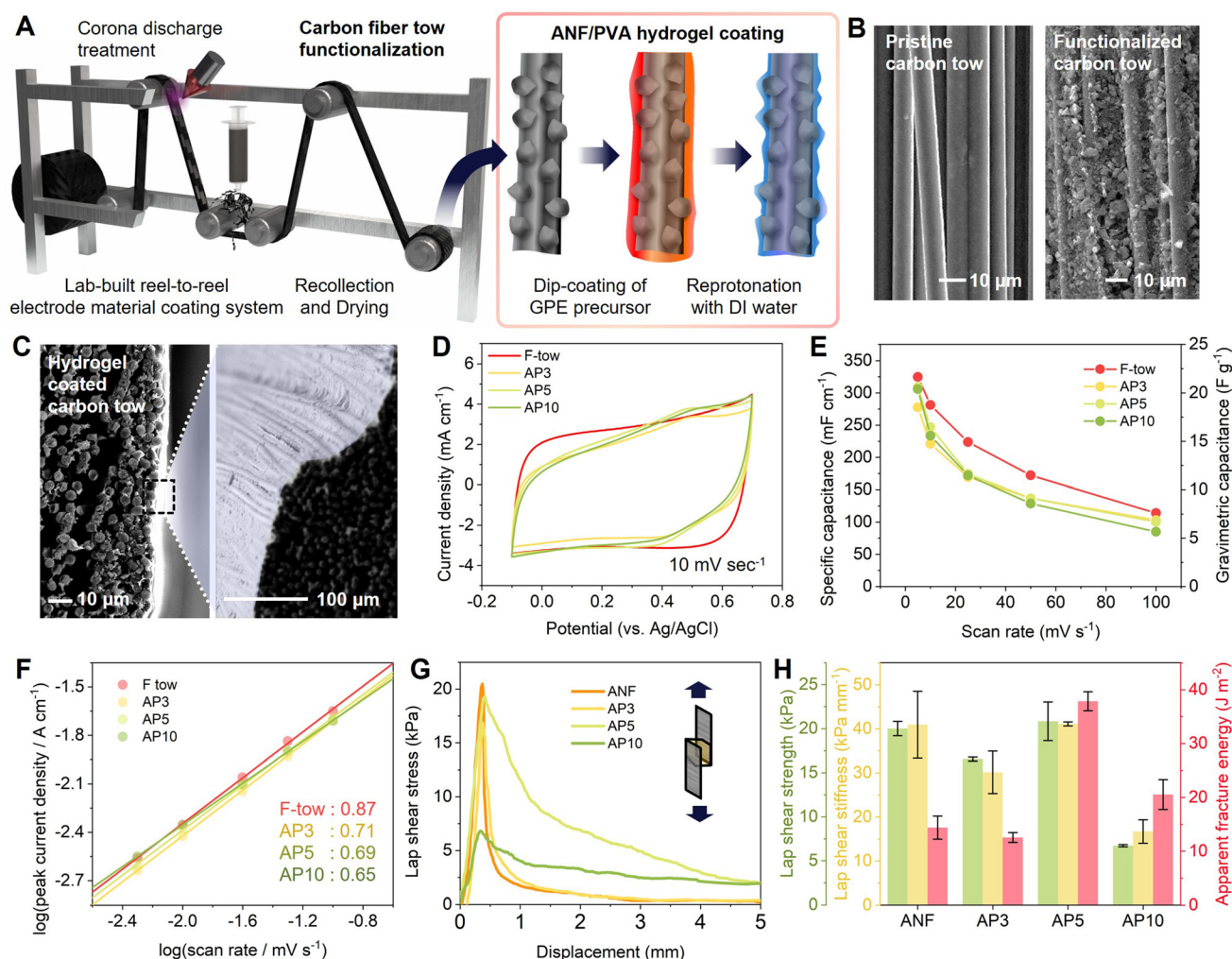
Fig. 2 (A) Schematic illustration of AC-functionalized carbon fiber tows with subsequent ANF–PVA hydrogel coating. (B) SEM images of pristine and AC-functionalized carbon fiber tows. (C) SEM images of F-tows coated with AP hydrogel coating. (D) Cyclic voltammograms of uncoated and AP-coated F-tow electrodes measured at 10 mV s⁻¹. (E) Scan-rate-dependent specific and gravimetric capacitances and (F) *b*-values obtained from power-law analysis of CV data. (G) Lap shear stress−displacement curves of F-tows bonded with ANF and AP hydrogels. (H) Summary of interfacial adhesion performance for different hydrogel compositions.

Briefly, the device was fabricated by coating F-tows with the AP5 hydrogel, followed by electrolyte impregnation in a 25 wt% LiCl aqueous solution to form GPE layers, after which two GPE-coated tows were assembled in a parallel configuration. The detailed fabrication procedure is provided in the Experimental section. In this architecture, the AP5 hydrogel functions as a continuous GPE that simultaneously separates the two electrodes and enables ionic transport between them, eliminating the need for an additional separator layer.

The electrochemical stability window of the fabricated fiber-shaped supercapacitor was evaluated by CV while gradually expanding the operating voltage from 0.6 to 1.6 V to probe the onset of redox reactions (Fig. 3B). GCD tests were also performed at each voltage window to assess coulombic efficiency, and the corresponding profiles are provided in Fig. 3C. As shown in the CV curves, no discernible redox peaks associated

with parasitic faradaic reactions were observed across the investigated voltage range, even when the upper voltage limit was extended to 1.6 V, indicating the absence of pronounced faradaic processes. However, considering coulombic efficiency, a voltage window of 0.8 V was selected for subsequent evaluations, within which the device exhibited stable operation with coulombic efficiency exceeding 99%.

To quantitatively evaluate the operability and electrochemical performance of the fabricated device over a wide temperature range, EIS, CV, and GCD measurements were performed at −20, 0, 25, and 50 °C. Fig. 3D presents the Nyquist plots obtained from EIS analysis at the corresponding temperatures. As the temperature decreases, the high-frequency intercept, which reflects the overall series resistance of the device, exhibits only a modest increase from 11.8 to 32.9 Ω when the temperature is reduced from 50 to −20 °C. Such a
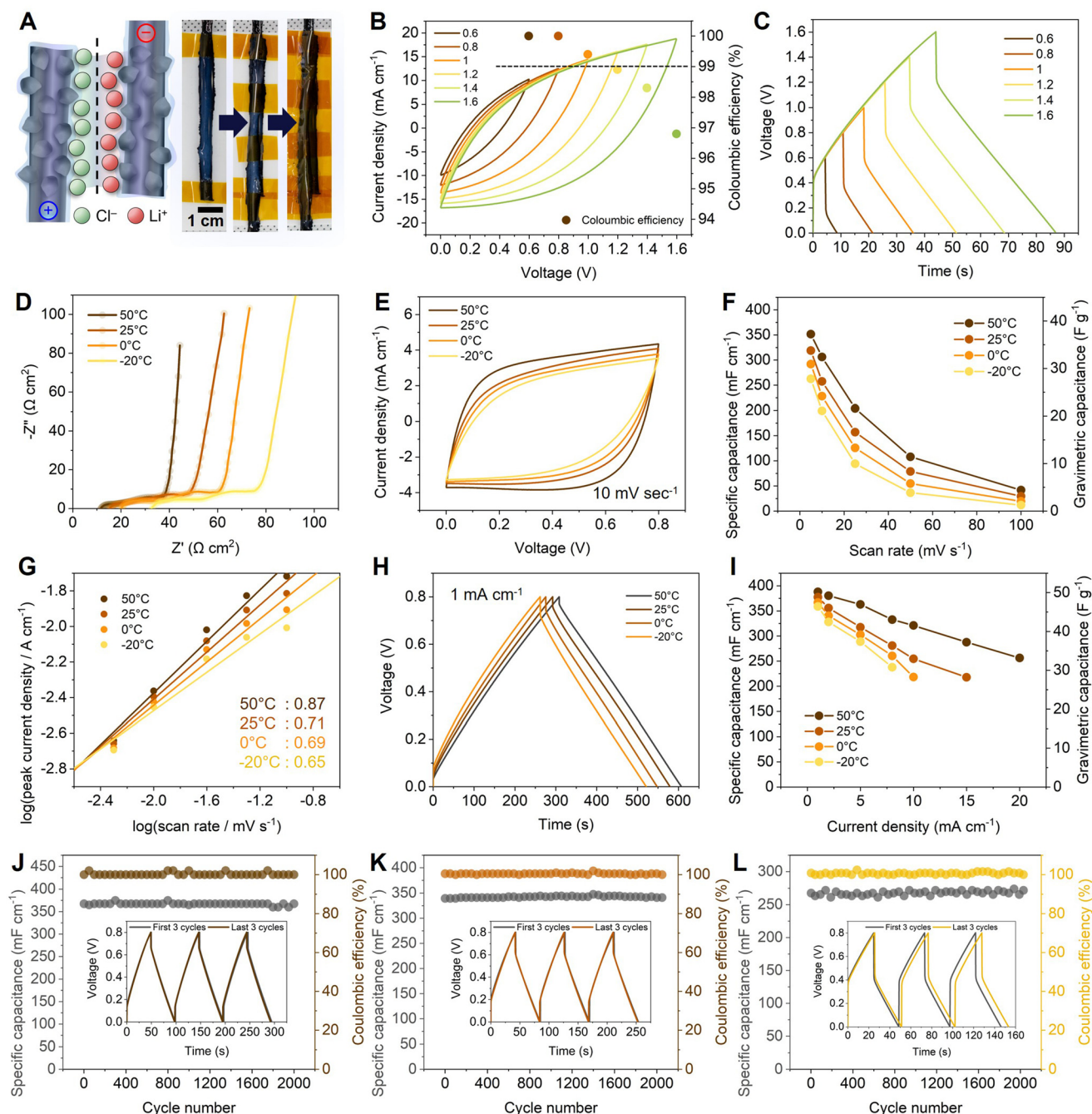
Fig. 3 (A) Schematic illustration and optical images of the fiber-shaped supercapacitor fabricated using AP5-based GPE. (B) CV curves acquired at different operating voltage windows and (C) corresponding GCD profiles used to evaluate the electrochemical stability window. (D) Nyquist plots obtained from EIS measurements at different temperatures. (E) CV curves recorded at various temperatures and (F) corresponding temperature-dependent specific and gravimetric capacitances. (G) Temperature-dependent *b*-values derived from CV analysis. (H) GCD profiles measured at different temperatures and (I) corresponding rate-dependent specific capacitances. (J–L) Long-term cycling stability of the fiber-shaped super-capacitor evaluated at 50, 25 and −20 °C, respectively.

limited variation in series resistance suggests that efficient ionic conduction is largely maintained within the device even under sub-zero conditions.

Subsequently, CV measurements were conducted to examine the electrochemical stability of the device and the possible occurrence of side reactions at different temperatures.

As shown in Fig. 3E, no discernible redox peaks or additional features associated with parasitic faradaic reactions are observed over the entire temperature range investigated. Comparison of the CV curves further shows that the quasi-rectangular profiles are largely preserved as the temperature decreases, with only slight rounding at lower temperatures.

The corresponding specific and gravimetric capacitances derived from the CV curves are summarized in Fig. 3F for scan rates ranging from 5 to 100 mV s^{-1} (full datasets are provided in Fig. S6). Although both capacitance values decrease with decreasing temperature, the device retains appreciable charge-storage capability even at -20 °C, delivering a specific capacitance of 262.6 mF cm^{-1} and a gravimetric capacitance of 27.8 F g^{-1} at a scan rate of 5 mV s^{-1}.

The temperature-dependent kinetic behavior was further quantified by calculating the b-values at each temperature (Fig. 3G). At elevated temperature, a relatively high b-value of 0.87 indicates predominantly surface-controlled capacitive charge storage. As the temperature decreases, the b-value decreases to 0.65 at -20 °C, reflecting an increased contribution from diffusion-influenced kinetics within the AP GPE layer. This variation is attributed to temperature-dependent changes in ion transport kinetics, consistent with the temperature-dependent impedance response observed in the EIS analysis. Overall, the combined EIS, CV, and b-value analyses demonstrate that the fiber-shaped supercapacitor incorporating the AP GPE preserves stable capacitive behavior and efficient ion transport over a wide temperature range, including sub-zero conditions.

To further evaluate the low-temperature operability and energy-storage performance of the fabricated device, GCD and long-term cycling stability tests were conducted. Fig. 3H presents representative GCD profiles recorded at a current density of 1.0 mA cm^{-1} under various temperature conditions (additional GCD data over a current-density range of 1.0 to 20 mA cm^{-1} are provided in Fig. S7). The GCD curves retain nearly symmetric charge–discharge characteristics across the investigated temperature range, confirming reversible capacitive operation. As the temperature decreases, a gradual shortening of the charge–discharge time is observed, indicating a reduction in capacitance at lower temperatures.

The corresponding specific capacitance values extracted at different current densities (Fig. 3I) show that, while higher temperatures favor enhanced capacitance and rate capability, a substantial fraction of the room-temperature performance is preserved at low temperatures. This behavior is consistent with the temperature-dependent ion-transport characteristics discussed earlier and demonstrates that the AP GPE enables reliable energy-storage operation over a broad temperature window.

Long-term cycling stability tests were conducted at 50, 25, and -20 °C to evaluate the electrochemical durability of the fabricated device under repeated charge–discharge operation. As shown in Fig. 3J–L, the device maintains stable electrochemical performance with negligible capacitance decay over 2000 cycles at all tested temperatures; elevated temperature 50 °C (Fig. 3J), room temperature 25 °C (Fig. 3K), and sub-zero conditions -20 °C (Fig. 3L). At room temperature, extended cycling up to 10 000 cycles further confirms stable charge–discharge performance (Fig. S8). These results demonstrate that the device incorporating the AP GPE exhibits robust cycling stability and reliable operation over a wide temperature range.
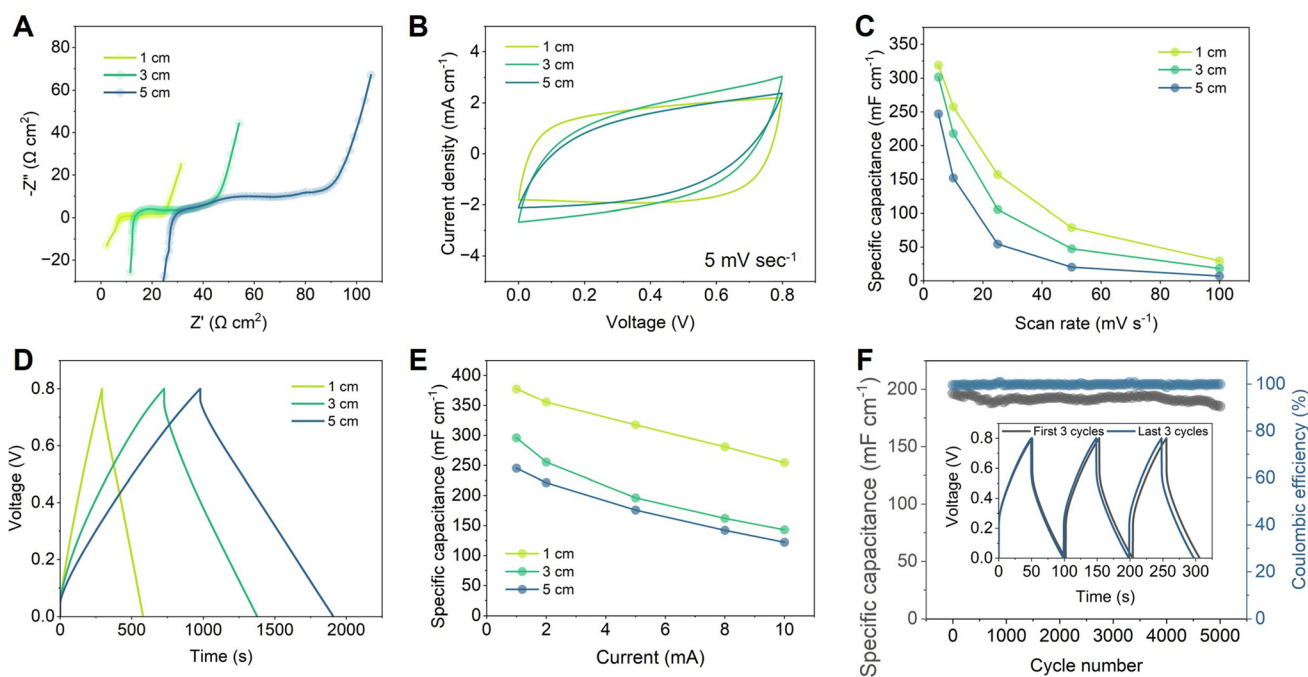

Fig. 4 (A) Nyquist plots of fiber-shaped supercapacitors with different device lengths. (B) Representative CV curves recorded at 5 mV s^{-1} for devices of different lengths. (C) Scan-rate-dependent, length-normalized specific capacitance. (D) Representative GCD profiles recorded at 1.0 mA for devices with different lengths. (E) Length-normalized specific capacitance as a function of discharge current. (F) Long-term cycling stability of the 5 cm device over 5000 charge–discharge cycles.

In addition, as summarized in Fig. S9 and Table S5, the areal specific capacitance of the present AP GPE-based device is superior to that of previously reported fiber-shaped supercapacitors at comparable current densities.

To verify the longitudinal scalability of the fiber-shaped supercapacitor, devices with lengths of 1.0, 3.0, and 5.0 cm were fabricated using identical electrode architectures and AP GPE coating conditions. Their electrochemical behavior was systematically evaluated as a function of device length. Fig. 4A presents the Nyquist plots obtained from EIS measurements. As the device length increases, the series resistance increases almost linearly from 7.5 Ω for 1.0 cm to 13.6 Ω for 3.0 cm and 28.2 Ω for 5.0 cm. When normalized by device length, the series resistance remains nearly constant at an average value of $\sim$5.2 Ω cm^{-1} (Fig. S10), indicating uniform electrochemical characteristics and effective longitudinal scalability.

Representative CV curves recorded at a scan rate of 5.0 mV s^{-1} for devices of different lengths are shown in Fig. 4B, with the full scan-rate-dependent CV data provided in Fig. S11. While the CV profiles become slightly more rounded with increasing length, all devices exhibit quasi-rectangular CV profiles characteristic of capacitive behavior. The corresponding scan-rate-dependent, length-normalized specific capacitances are provided in Fig. 4C. Although the specific capacitance decreases gradually with increasing length, the reduction remains moderate, decreasing from 39.9 F g^{-1} for the 1.0 cm device to 30.9 F g^{-1} for the 5.0 cm device at a scan rate of 5 mV s^{-1}.

Length-dependent capacitive performance was further examined by GCD measurements. Representative GCD profiles recorded at a current of 1.0 mA are shown in Fig. 4D, with specific capacitance values extracted over a current range of 1.0 to 10 mA summarized in Fig. 4E (full datasets are provided in Fig. S12). The discharge time increases systematically with device length, indicating that the total capacitance scales with the increased active electrode area of longer fibers, as expected for linearly extended electric double layer capacitor (EDLC) architectures. When normalized by device length (Fig. 4E), the specific capacitance decreases with increasing fiber length, accompanied by a gradual reduction in rate capability, which is attributed to increased electronic and ionic transport distances along the fiber axis.

Finally, the long-term cycling stability of the 5 cm device was evaluated at room temperature. As shown in Fig. 4F, the device retains more than 90% of its initial capacitance after 5000 charge–discharge cycles, demonstrating stable electrochemical performance under prolonged operation. These results confirm that the present fiber-shaped EDLC architecture maintains robust capacitive behavior even at the longest device length investigated, supporting its suitability for scalable fiber-based energy-storage applications.

form for separator-free, fiber-shaped aqueous supercapacitors. The GPE architecture integrates a rigid, percolating ANF scaffold with a hydrophilic PVA phase, enabling mechanical reinforcement through reversible hydrogen bonding while preserving hydrated ion-transport pathways. Systematic characterization shows that PVA incorporation enhances deformability, toughness, and interfacial adhesion *via* polymer-mediated bridging between adjacent ANFs, while maintaining continuous ion-transport pathways and sufficient ionic conductivity. Fiber-shaped supercapacitors incorporating the optimized AP5 GPE exhibit stable electrochemical operation over a wide temperature range, including sub-zero conditions, with robust cycling stability and preserved capacitive behavior. Device-length-dependent studies further confirm good longitudinal scalability. Overall, this work highlights composite nanofiber–polymer architectures as an effective strategy for balancing mechanical integrity, interfacial stability, and ion transport in gel electrolytes for scalable and wearable energy-storage systems.

Author contributions

Yuseung Choi and Gilyong Shin: conceptualization, methodology, investigation, formal analysis, visualization, writing – original draft. Eun Jae Nam: visualization, validation. Ji Heon Hong: investigation, validation. Byeong Jun So: formal analysis, methodology. Tae June Kang: supervision, project administration, funding acquisition, writing – review & editing.

Conflicts of interest

There are no conflicts to declare.

Data availability

The data supporting this article are included in the supplementary information (SI). Supplementary information: additional characterization and electrochemical data, including digital images and AFM analysis of aramid nanofibers, optical images of ANF–PVA hydrogels, full FT-IR spectra, thermogravimetric and elemental analyses, and detailed mechanical testing results. It also contains extended electrochemical measurements, including cyclic voltammetry and galvanostatic charge–discharge profiles acquired over a wide range of scan rates, current densities, temperatures, and device lengths, as well as supplementary impedance analysis supporting the length-dependent scalability of the devices. See DOI: https://doi.org/10.1039/d6nr00226a.

4. Conclusions

In this work, we demonstrate an ANF–PVA composite GPE that provides a mechanically resilient and ionically accessible plat-

Acknowledgements

References

1 B.-H. Xiao, K. Xiao, J.-X. Li, C.-F. Xiao, S. Cao and Z.-Q. Liu, *Chem. Sci.*, 2024, **15**, 11229–11266.

2 K. Keum, J. W. Kim, S. Y. Hong, J. G. Son, S. S. Lee and J. S. Ha, *Adv. Mater.*, 2020, **32**, 2002180.

3 X. Gong, Q. Yang, C. Zhi and P. S. Lee, *Adv. Energy Mater.*, 2021, **11**, 2003308.

4 J. Ding, Y. Yang, J. Poisson, Y. He, H. Zhang, Y. Zhang, Y. Bao, S. Chen, Y. M. Chen and K. Zhang, *ACS Energy Lett.*, 2024, **9**, 1803–1825.

5 R. Qi, W. Tang, Y. Shi, K. Teng, Y. Deng, L. Zhang, J. Zhang and R. Liu, *Adv. Funct. Mater.*, 2023, **33**, 2306052.

6 Z. Zhao, Z. Xu, Y. Wang, W. Huang, Y. Cheng and W.-Y. Wong, *J. Mater. Chem. A*, 2025, **13**, 13175–13185.

7 Z. Li, J. Fu, X. Zhou, S. Gui, L. Wei, H. Yang, H. Li and X. Guo, *Adv. Sci.*, 2023, **10**, 2201718.

8 D. G. Mackanic, X. Yan, Q. Zhang, N. Matsuhisa, Z. Yu, Y. Jiang, T. Manika, J. Lopez, H. Yan and K. Liu, *Nat. Commun.*, 2019, **10**, 5384.

9 B. Yiming, Z. Jia and C. Creton, *Chem. Rev.*, 2025, **125**, 10457–10491.

10 X. Deng, J. Chen, X. Jia, X. Da, Y. Zhao, Y. Gao, Y. Gao, X. Kong, S. Ding and G. Gao, *Angew. Chem.*, 2024, **136**, e202410818.

11 S. Huang, L. Hou, T. Li, Y. Jiao and P. Wu, *Adv. Mater.*, 2022, **34**, 2110140.

12 C. Lu and X. Chen, *Nano Lett.*, 2020, **20**, 1907–1914.

13 W. Zhu, Z. Lei and P. Wu, *Energy Environ. Sci.*, 2025, **18**, 3647–3658.

14 S. W. Song, H. Kim, S. Shin, S. Jang, J. H. Bae, C. Pang, J. Choi and K. R. Yoon, *Energy Storage Mater.*, 2023, **60**, 102802.

15 Y. Fu, Z. Gu, Q. Gan and Y.-W. Mai, *Mater. Sci. Eng., R*, 2024, **160**, 100815.

16 L. Suo, O. Borodin, T. Gao, M. Olguin, J. Ho, X. Fan, C. Luo, C. Wang and K. Xu, *Science*, 2015, **350**, 938–943.

17 F. Wang, O. Borodin, T. Gao, X. Fan, W. Sun, F. Han, A. Faraone, J. A. Dura, K. Xu and C. Wang, *Nat. Mater.*, 2018, **17**, 543–549.

18 D. Yen, C.-H. Lin, D. J. Sprouster, X. Zheng, X. Xiao, W.-K. Lee, M. Ge and Y.-c. K. Chen-Wiegart, *ACS Mater. Lett.*, 2023, **5**, 1466–1475.

19 D. Kasprzak, Z. Wu, L. Tao, J. Xu, Y. Zhang and J. Liu, *ACS Appl. Mater. Interfaces*, 2024, **16**, 36304–36314.

20 Y. Zhang and P. S. Cremer, *Curr. Opin. Chem. Biol.*, 2006, **10**, 658–663.

21 X. Chen, T. Yang, S. Kataoka and P. S. Cremer, *J. Am. Chem. Soc.*, 2007, **129**, 12272–12279.

22 G. Shin, J. Y. Baek, J. H. Kim, J. H. Lee, H. J. Kim, B. J. So, Y. Choi, S. Yun, T. Kim and J. G. Jeon, *Adv. Funct. Mater.*, 2025, **35**, 2412524.

23 M. Yang, K. Cao, L. Sui, Y. Qi, J. Zhu, A. Waas, E. M. Arruda, J. Kieffer, M. Thouless and N. A. Kotov, *ACS Nano*, 2011, **5**, 6945–6954.

24 B. Yang, L. Wang, M. Zhang, J. Luo and X. Ding, *ACS Nano*, 2019, **13**, 7886–7897.

25 H.-J. Chen, Q.-Y. Bai, M.-C. Liu, G. Wu and Y.-Z. Wang, *Green Chem.*, 2021, **23**, 7646–7658.

26 Z. J. Chen, T. Y. Shen, X. Xiao, X. C. He, Y. L. Luo, Z. Jin and C. H. Li, *Adv. Mater.*, 2024, **36**, 2413268.

27 L. Xu, X. Zhao, C. Xu and N. A. Kotov, *Adv. Mater.*, 2018, **30**, 1703343.

28 D. Parisi, C. D. Ditillo, A. Han, S. Lindberg, M. W. Hamersky and R. H. Colby, *J. Rheol.*, 2022, **66**, 1141–1150.

29 X. Yu, Y. Fu, X. Cai, H. Kafafy, H. Wu, M. Peng, S. Hou, Z. Lv, S. Ye and D. Zou, *Nano Energy*, 2013, **2**, 1242–1248.

30 S. Xu, P. Shen, Z. Shen, R. Chen, D. Zhang, Z. Zhao, Y. Zhang, D. Li, Y. Xiong and X. Wang, *Chem. Eng. J.*, 2025, **504**, 158509.

31 R. Gray, T. Barthelay, C. R. Bowen, F. Marken, A. J. Lunt, L. E. Asp, D. Zenkert, P. S. Rodriguez, J. Xu and K. Bouton, *J. Mater. Chem. A*, 2024, **12**, 25580–25599.

32 S. Zhai, W. Jiang, L. Wei, H. E. Karahan, Y. Yuan, A. K. Ng and Y. Chen, *Mater. Horiz.*, 2015, **2**, 598–605.

33 H. Zhou, Y. Su, J. Zhang, H. Li, L. Zhou and H. Huang, *Chem. Eng. J.*, 2023, **454**, 140222.

34 B. J. So, G. Shin, Y. Choi, H. Lee, J. G. Jeon and T. J. Kang, *Funct. Compos. Struct.*, 2025, **7**, 015005.

35 J. Zhou, X. Liu, X. He, H. Wang, D. Ma and X. Lu, *Polymers*, 2022, **15**, 141.

36 J. Fan, Z. Shi, L. Zhang, J. Wang and J. Yin, *Nanoscale*, 2012, **4**, 7046–7055.

37 J. Zhu, M. Yang, A. Emre, J. H. Bahng, L. Xu, J. Yeom, B. Yeom, Y. Kim, K. Johnson and P. Green, *Angew. Chem., Int. Ed.*, 2017, **56**, 11744–11748.

38 L. Li, G. Yang, J. Lyu, Z. Sheng, F. Ma and X. Zhang, *Nat. Commun.*, 2023, **14**, 8450.

39 D. Lee, J. Cho, J. G. Son and B. Yeom, *Composites, Part B*, 2022, **229**, 109467.

40 L. Ding, D. Xiao, Z. Zhao, Y. Wei, J. Xue and H. Wang, *Adv. Sci.*, 2022, **9**, 2202869.

41 T. Steiner, *Angew. Chem., Int. Ed.*, 2002, **41**, 48–76.

42 X.-W. Wang, Z.-M. Hu and Z.-F. Liu, *Int. Polym. Process.*, 2008, **23**, 81–87.

43 A. Z. Sarsenbekova, U. B. Tuleuov, A. T. Kazhmuratova, A. N. Bolatbay, L. Z. Zhaparova and Y. M. Tazhbayev, *Polymers*, 2025, **17**, 2805.

44 Z. Peng and L. X. Kong, *Polym. Degrad. Stab.*, 2007, **92**, 1061–1071.

45 H. Zhu, S. Zhu, Z. Jia, S. Parvinian, Y. Li, O. Vaaland, L. Hu and T. Li, *Proc. Natl. Acad. Sci. U. S. A.*, 2015, **112**, 8971–8976.

46 J.-Y. Sun, X. Zhao, W. R. Illeperuma, O. Chaudhuri, K. H. Oh, D. J. Mooney, J. J. Vlassak and Z. Suo, *Nature*, 2012, **489**, 133–136.

47 J. P. Gong, *Soft Matter*, 2010, **6**, 2583–2590.